Fast phase error calibration through radix-p optimization processing

JIUN-YU SUNG[1,*] AND SAN-LIANG LEE[1]

[1] *Department of Electronic and Computer Engineering and Graduate Institute of Electro-Optical Engineering, National Taiwan University of Science and Technology, Taipei 106, Taiwan.*
*jysung@mail.ntust.edu.tw

Abstract: Optical phased arrays (OPAs) have been a popular option to manipulate the spatial behavior of the free-space optical beams. Inspired by the success of the integrated circuits (IC) industry, photonic IC (PIC) based OPAs have been actively studied in the last decade. Due to the fabrication imperfection, light passing through different paths typically results in random phase errors. The phase errors can seriously deviate the interference pattern of an OPA, and radically change the spatial distribution of the optical field. This phenomenon will significantly degrade the performance for applications like image scanning and optical wireless communication (OWC). Thermally or electrically tunable phase shifters can be applied to compensate the phase errors through dedicated calibration algorithms. However, the complexity of the calibration processes quickly increases with the number of the OPA's elements. Hence, the whole processing can be time-consuming and this significantly pushes the overall system cost. Besides, considering the potential dynamic factors such as thermal gradient and aging effects, continuous calibration may be necessary. This results in great demand for fast and efficient calibration processing for the practical applications. In this paper, novel and efficient radix-p calibration processing is proposed which can be directly combined with most of the already reported/developed optimization algorithms as a speed-up turbo. It is shown that the computation time of the proposed radix-p processing grows linearly with the number of the OPA's elements. In comparison to the conventional particle swarm optimization (PSO) algorithm, which exhibits exponential computation time in our numerical results, the radix-p processing shows great efficiency improvement. In the numerical results, speed with more than 12 times faster is shown for the proposed radix-p processing compared to the traditional PSO algorithms.

1. Introduction

Information and communication technology (ICT) is rapidly developed. It has been widely discussed that the traditional all-electronic solutions may be insufficient for the ever stringent I/O interconnection requirement. Inspired by the success of the integrated circuits (IC) industry and the practical demand for faster interconnection, photonic IC (PIC) technologies are actively studied and developed in the last decades. With the growing momentum of the PIC industry, tremendous trials/tests of applying PIC to various applications have also been extensively performed.

Free-space optics is crucial for applications like optical wireless communication (OWC), light detection and ranging (LiDAR), and image scanning. For their advantages of programmability and flexibility, optical phased arrays (OPAs) become a popular option for manipulating the free-space optical beams. A simple OPA architecture built on silicon photonics is introduced in 2009 [1]. Since then, many PIC based OPAs have been implemented in various platforms, and their performance and scales are quickly improved [2-10]. More detailed illustration of the background and comparisons for different state-of-the-art works can be found in [5, 9, 11]. Due to the potential fabrication imperfection, the optical signals passing through different waveguides/paths typically result in random phase errors. These phase errors can seriously deviate the interference pattern of an OPA, and radically change the spatial

48 distribution of the optical field. The resultant beams are typically broadened and have poor
49 directivity; hence greatly deteriorate the scanning and transmission performance. The problems
50 are commonly solved by applying thermally or electrically tunable phase shifters to calibrate
51 the phase errors after the fabrication of the OPAs [2-11].
52   A feedback sub-system is typically applied for the calibration processes. Specific beam
53 parameters are monitored and the phase shifters are tuned according to the corresponding
54 responses until the best beam performance is detected. Pre-calibration can be performed for the
55 factory OPAs by using the images detected by remote cameras as the feedback signals. Real-
56 time calibration can be performed by monitoring the feedback signals of additional on-chip
57 detectors as Ref. [3, 12]. As the solution set of all possible phase states exponentially increases
58 with the number of the OPA's elements [12], it is surely inefficient to perform the calibration
59 through nested sweeps over all the possible phase states. Many optimization algorithms have
60 been proposed to reduce the time consumption of the calibration processes. Hill climber [2, 4]
61 and gradient descent (GD) [8] are two common algorithms for the optimization problems.
62 However, as the phase error calibration is not a convex problem, local extreme uncertainty may
63 exist. While the number of antenna elements increases, extra processing time for sequentially
64 querying the responses from different antenna elements (channels) may also be significant.
65 Stochastic parallel gradient descent (SPGD) is a variant algorithm which can get the stochastic
66 gradient though a single-step calculation [12]. Hence, the time expended on the sequential
67 querying processes can be saved. Based on SPGD, a two-stage algorithm named deterministic-
68 stochastic gradient descent (DSGD) is proposed in [12]. DSGD first coarsely adjusts the OPA
69 with a smaller possible solution set. This tunes the OPA to be at phase states close to the optimal
70 solution. Then SPGD is applied to derive the final optimal solution. According the published
71 results, DSGD can efficiently mitigate the local extreme uncertainty problems, and get accurate
72 results of the optimal points. Particle swarm optimization (PSO) [3] and genetic algorithm (GA)
73 [10] have also been common options for the phase error calibration. These algorithms are more
74 resistant to local extreme traps. In [10] and [12], it is shown that these two algorithms typically
75 can more quickly and accurately get the optimal solutions compared to the GD and hill-climber
76 based options. Though these algorithms have shown tremendous efficiency improvement
77 compared to the nested sweeps, the increasing computation time for a large OPA can still be a
78 cost concern. On the other hand, as the OPAs may work at different environment conditions,
79 calibration needs to be constantly performed to dynamically adjust its best driving parameters.
80 Hence, it is highly desirable to further push the efficiency of the algorithms. In [13], a modified
81 rotating element electric field vector (mREV) method is proposed. This algorithm shows great
82 potential in enhancing the computation efficiency. However, the in-phase condition cannot be
83 exactly guaranteed (though could eventually reach after sufficient iterations in a theoretical
84 viewpoint of the gradually reduced average errors). Moreover, according to the histograms of
85 [13], the final phase deviation as high as >30º can still exist after the calibration processes.
86   In this paper, novel and efficient radix-p calibration processing is proposed. The proposed
87 scheme can be directly combined with most of the already reported/developed optimization
88 algorithms as a speed-up turbo. It is shown that the computation time of the proposed radix-p
89 processing grows linearly with the number of the OPA's elements. In comparison to the
90 conventional particle swarm optimization (PSO) algorithm exhibiting exponential computation
91 time (according to the numerical results), the radix-p processing shows great efficiency
92 improvement. The basic concept of the proposed radix-p processing is to transform the
93 optimization problems for a large antenna array into much simplified optimization problems
94 for smaller sub-arrays composed of less antenna elements. Compared to other schemes (e.g.
95 mREV) building on similar concepts, the results derived by the proposed radix-p method
96 theoretically match with the exact optimal point. Slight final error are observed, which may
97 mainly come from the numerical limitation. The errors majorly influence the field pattern at
98 regions several tens of dB lower than the main peak. Considering the potential noise levels, this
99 may only cause negligible degradation of the systems. In the numerical results, ~13.256 dB
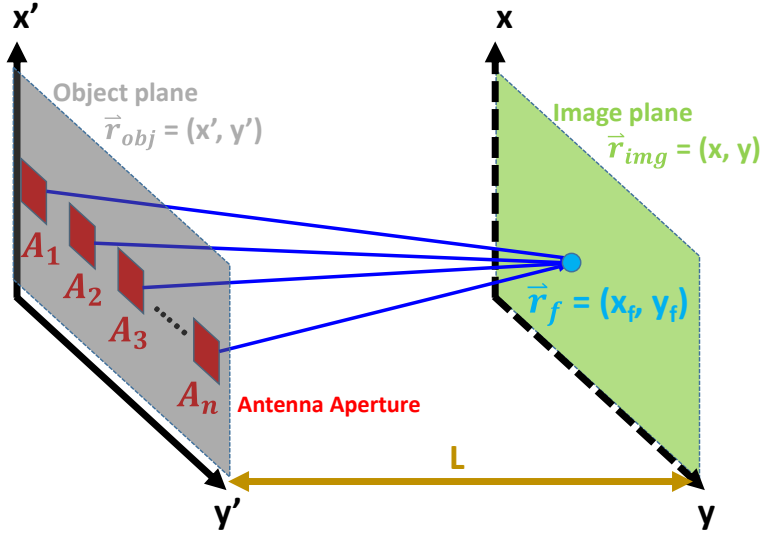
Fig. 1. The imaging coordinate system.

100 side-mode suppression ratio (SMSR) is obtained for the uniformly spaced OPA and more than
101 12 times efficiency improvement is shown for the proposed radix-p processing compared to the
102 traditional PSO algorithms for an OPA with 64 elements.

103 ## 2. Algorithm

104 An imaging system composed of an antenna array with N elements is considered as shown in
105 Fig. 1. The antenna array is located on the object plane, which is described by the coordinate
106 system of $\vec{r}_{obj}$ = (x', y'). The emission field of the n-th antenna element is denoted as
107 $\Phi_n(\vec{r}_{obj})e^{i\cdot\phi_n}$. Considering general cases allowing arbitrary emission patterns, $\Phi_n(\vec{r}_{obj})$ can be
108 a complex number. However, ϕ_n is purposely separated from $\Phi_n(\vec{r}_{obj})$ to describe the phase
109 errors. ϕ_n is the variable that will be adjusted for the calibration or beam-steering processes.
110 The emitted beam is monitored by a virtual image plane described by the coordinate system of
111 $\vec{r}_{img}$ = (x, y). The image plane is parallel to the object plane with a separation distance of L.
112 According to the Fraunhofer approximation, the observed image pattern can be expressed as:

$$\Psi(\vec{r}_{img}) = \frac{i}{\lambda L}e^{-i\frac{2\pi L}{\lambda}\left(1+\frac{|\vec{r}_{img}|^2}{2L^2}\right)}\sum_{n=1}^{N}e^{i\phi_n}\int_{A_n'}\Phi_n(\vec{r}_{obj})e^{i2\pi\frac{\vec{r}_{img}\cdot\vec{r}_{obj}}{\lambda L}}dA_n', \qquad (1)$$

114 where A_n' is the area occupied by the n-th antenna element and λ is the operation wavelength.
115 In the calibration processes, a specific point ($\vec{r}_f$) on the image plane which denotes the
116 direction of the steered beam is concerned. ϕ_n is adjusted to get maximum intensity at $\vec{r}_f$, so
117 that the emission power is maximally concentrated on the steering direction. After the integral
118 operation, the geometrical factors of the antenna elements can be separated. Then the overall
119 field at $\vec{r}_f$ can be considered as composition of discrete radiators from the antenna elements as:

120
$$\Psi\left(\bar{r}_f\right) = \sum_{n=1}^{N} Y_n\left(\bar{r}_f\right) e^{i\left(\xi_n\left(\bar{r}_f\right)+\phi_n\right)} . \tag{2}$$

121     $Y_n\left(\bar{r}_f\right)$ and $\xi_n\left(\bar{r}_f\right)$ are both functions of $\bar{r}_f$. For simplicity, they will be directly denoted as

122   Y_n and ξ_n. ϕ_n is kept separated from ξ_n for the succeeding optimization processes.

123   According to the triangular inequality, the maximum intensity at $\bar{r}_f$ can be estimated as:

124
$$I\left(\bar{r}_f\right) = \left|\Psi\left(\bar{r}_f\right)\right|^2 = \left|\sum_{n=1}^{N} Y_n\left(\bar{r}_f\right) e^{i\left(\xi_n\left(\bar{r}_f\right)+\phi_n\right)}\right|^2 \leq \left|\sum_{n=1}^{N} Y_n\left(\bar{r}_f\right)\right|^2 = \left|e^{i\left(\phi_v\right)}\sum_{n=1}^{N} Y_n\left(\bar{r}_f\right)\right|^2 . \tag{3}$$

125   This obeys the instinctive results that the maximum intensity is obtained while all radiators are
126   in-phase. The calibration processes mainly work to adjust the phase terms shown in Eq. (2) to
127   meet this in-phase criterion. It should also be noted that as the in-phase criterion is set for the
128   optimization problem, the potential amplitude mismatches among antenna elements of practical
129   OPAs will theoretically have no influences for the optimization processing. As illustrated in
130   section 1, many algorithms (like GD, PSO, GA, etc.) can be applied for the calibration.
131   However, as N increases, the calibration time can significantly increase. This increases the
132   calibration cost and is disadvantageous for the applications requiring repeating calibrations to
133   adapt the environment variation or aging effects.
134   In our proposed radix-p algorithm, multi-layer processing is performed. In the initial
135   processing layer, the N antenna elements are grouped into M sub-sets. Each sub-set comprises
136   p distinguished antenna elements and is processed sequentially according to the index number
137   of the sub-sets. For better illustrating the following processes, p=2 is chosen as an example. In
138   order to distinguish the processing terms, the 1-st sub-set is separated from Eq. (2) as:

139
$$\Psi\left(\bar{r}_f\right) = Y_a e^{i\left(\xi_a+\phi_a\right)} + Y_b e^{i\left(\xi_b+\phi_b\right)} + \sum_{n=1,n\neq a,b}^{N} Y_n e^{i\left(\xi_n+\phi_n\right)} , \tag{4}$$

140   where a and b are respectively the indexes of the two antenna elements belonging to the 1-st
141   sub-set. In Eq. (4), the summation of the remaining N-2 complex numbers can be merged and
142   represented by another complex number as:

143
$$\Psi\left(\bar{r}_f\right) = Y_a e^{i\left(\xi_a+\phi_a\right)} + Y_b e^{i\left(\xi_b+\phi_b\right)} + K_s e^{i\cdot\phi_{s,1}} , \tag{5}$$

144   where K_s and $\phi_{s,1}$ respectively denotes the overall amplitude and phase of the antenna

145   radiators excluding the two antenna elements of the 1-th sub-set. Then the optimization
146   processing is performed by adjusting the two antenna elements of the 1-st sub-set to maximize
147   the intensity at $\bar{r}_f$. Again, according to the triangular inequality, the maximum intensity

148   observed at $\bar{r}_f$ is:

149
$$I\left(\bar{r}_f\right) = \left|\Psi\left(\bar{r}_f\right)\right|^2 \leq \left|Y_a + Y_b + K_s\right|^2 . \tag{6}$$

150   As the third term of Eq. (5) is not adjusted during the optimization processing, the final phases
151   of the two antenna elements must be equal to $\phi_{s,1}$, so that the equality of Eq. (6) holds. After

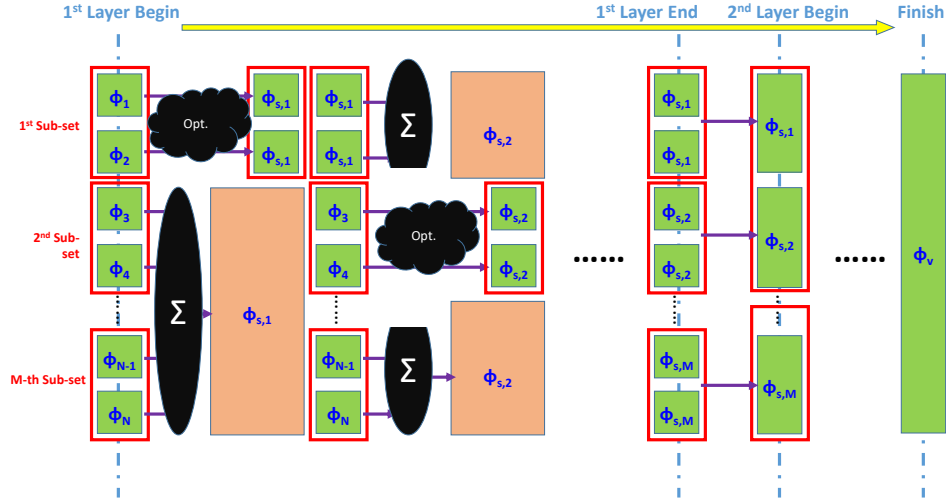152   finishing the processing for the 1-st sub-set, the resultant image field is then:

Fig. 2. Processing flows of the proposed radix-p algorithm. Opt.: optimization.

153

$$\Psi\left(\bar{r}_f\right) = Y_a e^{i\cdot\phi_{s,1}} + Y_b e^{i\cdot\phi_{s,1}} + K_s e^{i\cdot\phi_{s,1}}$$
$$= Y_{G,1} e^{i\cdot\phi_{s,1}} + K_s e^{i\cdot\phi_{s,1}}$$

(7)

154 In Eq (7), as the phase terms of the concerned sub-set are equal, they are further merged into a
155 single term $Y_{G,1} e^{i\cdot\phi_{s,1}}$. Next, the 2-nd sub-set is selected and the identical processing described
156 in Eq. (4)~(7) is performed. It is noted that as those sub-sets which are not concerned are merged
157 into the third term of Eq. (4), they will not be further adjusted while the m-th sub-set is
158 performing its optimization processing. After M=N/p (p=2 for this example) sub-set processing,
159 the 1-st layer processing finishes. Then the image field becomes:

160

$$\Psi\left(\bar{r}_f\right) = \sum_{n=1}^{N/p} Y_{G,n} e^{i\cdot\phi_{s,n}}$$

(8)

161 It can be observed that Eq. (8) and Eq. (2) have the identical form with the processing radiator
162 terms reduced by 1/p times (half for p=2). Hence, the processing illustrated in Eq. (4)~(8) can
163 be repeated for the 2-nd and every succeeding layer. It can be seen that for each new processing
164 layer, the processing terms and the number of phase differences are reduced to 1/p of the
165 previous layer. At the last layer, there will remain only one radiator term. Then all antenna
166 elements meet the in-phase criterion, and the whole calibration processing finishes.
167   Figure 2 summarizes the whole processing of the proposed algorithm for p=2. In the
168 beginning of the processing (1-st layer), the elements of the OPA have phase errors of $\phi_1 \sim \phi_N$.
169 Each two of the antenna elements are grouped and form M=N/2 sub-sets (each is circled by the
170 red line in the left side of Fig. 2). First, the 1-st sub-set is selected, and their phases are optimized
171 to get the maximum intensity for the interested point on the image plane. After the processing,
172 both antenna elements' phases are adjusted to $\phi_{s,1}$. This $\phi_{s,1}$ is identical to the phase value of
173 the overall field composed of the other N-2 antenna elements (as shown in the leftmost skin-
174 colored block). Next, the 2-nd sub-set is selected and processed by the same processing. The

175　final phases of the 2-nd sub-set will be $\phi_{s,2}$. Identical processing is sequentially and repeatedly

176　performed on all of the M sub-sets. At the end of the 1-st layer processing, the phases of the M

177　sub-sets become $\phi_{s,1} \sim \phi_{s,M}$. It is seen that both antenna elements of the same sub-set have the

178　same phases. These elements are then synchronized in values for every succeeding processing.
179　Hence, only half number of phases are needed to be adjusted for the next processing layer. The

180　processing continues layer-by-layer until there remains a single phase ϕ_v. Then all phases of

181　the antenna elements are perfectly in-phase, and the intensity on the point of interest is
182　guaranteed to be maximum.
183　　　Once all antenna elements are adjusted to be in-phase, further procedures may be performed
184　to estimate the relations between the phase states and the electrical control signals of each
185　antenna element. The antenna elements are sequentially selected to be tuned with different
186　electrical signal levels. At the tuning moments for a specific antenna element, all other elements
187　else are maintained intact. Hence, the relations between the feedback signals and the electrical
188　control signals can be detected. Then, according to the interference physics of light, the
189　relations between the phase states and the control signals can be estimated. To steer the beams
190　towards specific directions, the required phase states of each antenna element can be calculated
191　according to diffraction optics principles. Then the electrical control signals are tuned to the
192　corresponding levels for beam-steering.
193　　　It is noted that the free-space propagation delays of waves from different antenna elements
194　are included in the overall phases of the far fields as shown in Eq. (1) and (2). Hence, the above
195　beam-steering processing implicitly presumes the phase calibration is performed with the
196　feedback signal generated at the central (0-degree) direction. Practically, it is difficult to
197　accurately identify whether the feedback signals are from the central direction or not. Hence,
198　phase calibration processing may be performed at multiple beam angles. The relative beam
199　angles can be measured and used to estimate the additional phases generated from the
200　propagation delays. Then, the actual on-chip phase errors can be separated from the overall
201　phases estimated by the radix-p processing. It is also noted that the geometric positions of the
202　antenna elements are not restricted in Eq. (1) and (2). Hence, the radix-p processing can also
203　be applied to calibrate the phase errors of aperiodic OPAs. It can be seen that the propagation
204　optical path lengths, $d_i*\sin(\theta)$ for the i-th antenna element, become 0 at the central direction
205　with arbitrary values of d_i. Therefore, the in-phase condition is maintained for any geometric
206　arrangement of antennas. However, while the calibration feedback signals are detected off the
207　central direction, the degree of freedom introduced by the geometric factors can result in further
208　phase uncertainty. Hence, the geometric errors must be guaranteed within specific levels to
209　ensure the final on-chip phase errors are correctly estimated and calibrated.

3. Performance

211　Simulation and numerical calculation are performed to estimate the performance of the
212　proposed algorithm. The CPU equipped in the computer is i5-4590. A 2-D imaging system like
213　Fig. 1 is numerically built in MATLAB. Wavelength of 1.55 um is used in the simulation. The
214　size of each antenna element is 0.75 um and the neighbor elements are separated by 9.5 um.
215　The beam is detected 10 cm away from the antenna array. Initial phases between [0, 2π) are
216　randomly allocated to the antenna elements, as an emulation of the phase errors. The
217　performance purely relevant to the proposed algorithm is characterized. PSO is selected as the
218　benchmark to separate the potential local extreme issues. The maximal iteration of every PSO
219　processing is set as 500 to exclude the ambiguity between the convergence performance and
220　the execution time. Techniques proposed in [14, 15] are added to the PSO setup to enhance the
221　convergence capability at the final iterations. The number of antenna elements and the particles
222　are varied according to the analysis conditions. The proposed scheme is applied as the radix-p

223 (p ∈ {2, 8, 16}) version of PSO. The performance between algorithms of the traditional PSO
224 and our proposed radix-p scheme is analyzed.

3.1 Computation time

226 The PSO may suffer from the local extreme issues while the number of particles is insufficient.
227 In order to ensure the global extreme results are correctly derived, multiple runs applying
228 different numbers of particles are performed. For each run, the derived result is compared with
229 the ideal solution, and the required numbers of particles for different OPA sizes are
230 characterized as Fig. 3(a). It is observed that required particles exponentially increased with the
231 sizes of the OPA. We believe this comes from the fact that the solution space grows
232 exponentially with the number of antenna elements [12]. Though it is not required for the PSO
233 to densely sweep the whole solution space, Fig. 3(a) may reveal that the particle number must
234 be kept at specific levels to ensure sufficient probabilities for the particles to hit the optimal
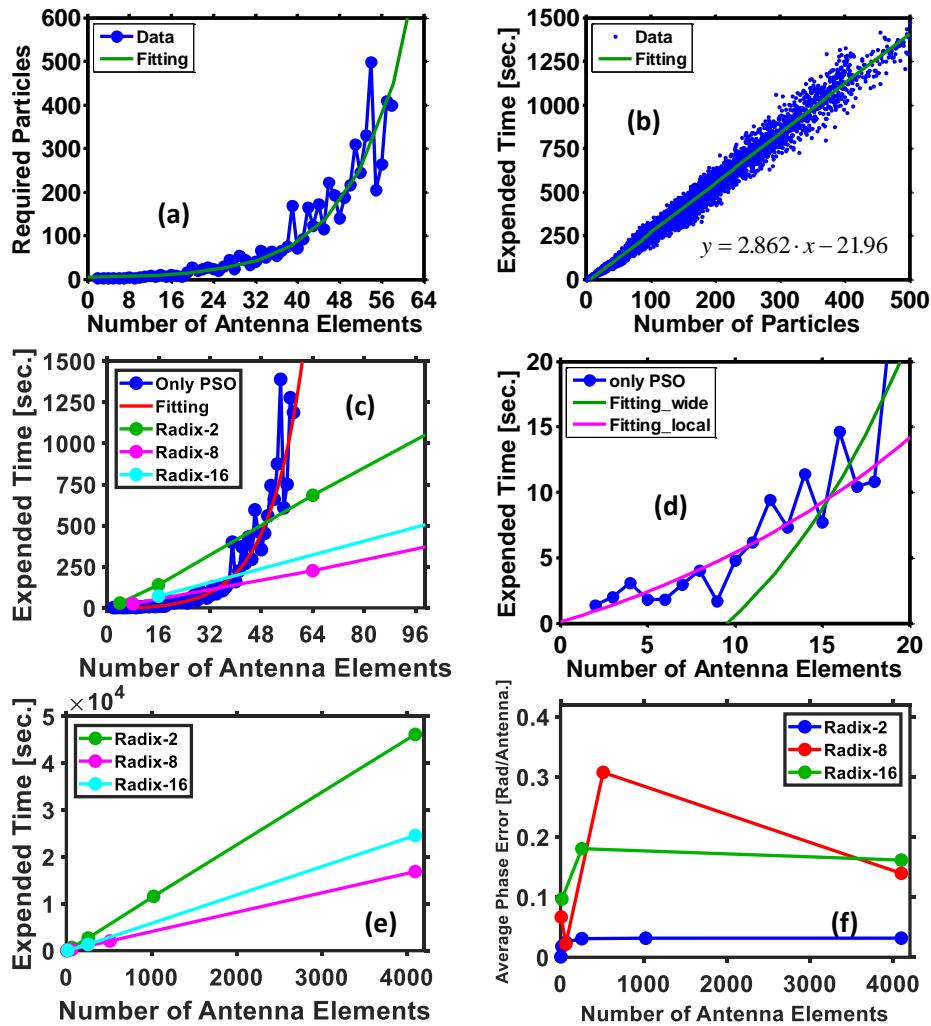

Fig. 3. Performance of the computation results. (a) Expended time for different number of particles. (b) Required
particles for getting the optimal solution. (c) Expended time for OPAs of different size. (d) Regionally enlarged
picture of (c) for the PSO curves. (e) Extended picture of (c) for the radix-p curves. (f) Calibrated errors.

Table 1. Coefficients of the Exponential Curves of Fig. 3

	Fitting function	a	b	c	Correlation
y = #Particle (Type I)	$y = a \cdot e^{b \cdot x} + c$	3.319	0.0827	-1.509	0.9809
y = Expended Time (Type I)	$y = a \cdot e^{b \cdot x} + c$	3.292	0.1016	-1.732	0.9842
y = #Particle (Type II)	$y = a \cdot e^{0.09234x} + c$	2.075	X	2.428	0.9868
y = Expended Time (Type II)	$y = a \cdot e^{0.09234x} + c$	5.539	X	-13.42	0.9898

Table 2. Coefficients of the Linear Curves of Fig. 3(c) and (e)

	Fitting function	Correlation
Radix-2	y=11.29 x - 52.12	~1
Radix-8	y=4.13 x – 30.03	~1
Radix-16	y=6.03 x - 118.11	~1

235 region. Hence, the required number of the particles increases with the solution space (antenna
236 elements). As a comparison, a particle number as high as 200 is applied in [12]. Fig. 3(b) shows
237 that the calculation time approximately grows linearly with the number of the applied particles.
238 We believe this mainly comes from the variable transferring latency, and could be much
239 reduced for practical systems. The corresponding execution time of the PSO optimization
240 processes is shown in Fig. 3(c), which also grows exponentially and meets the results of Fig.
241 3(a) and (b). Robust curve fitting is performed for the results shown in Fig. 3 through the
242 toolbox of MATLAB. The fitting results of Fig. 3(b) is directly labeled on the picture. The
243 regression results of Fig. 3(a) and (c) are discussed separately in Table 1. It is seen that two
244 different types of curve models are applied in Table 1. Type I is the generic form of the
245 exponential model. However, it is observed that coefficient "a" between Fig. 3 (a) and (c) are
246 similar (3.319 and 3.292). This obviously does not obey the linear relation observed in Fig. 3(b),
247 and could influence the accuracy for prediction of the required particles/execution time for
248 OPAs with larger sizes. Observable variations for the fitting results are also seen by changing
249 the initial conditions. We believe the errors mainly come from the sensitive features of the
250 exponential model. In order to reduce the errors, fitting model Type II is applied by fixing
251 coefficient "b" of the exponential model for both curves. Different "b" is locally swept
252 according to the results of Type 1, and the one with the highest correlation is chosen to be
253 0.09234. It is observed that the division between coefficient "a" of the two curves is 5.539/2.075
254 =2.669, which is closer to the slope of Fig. 3(b). We believe type II model more accurately
255 describes the results. According to the modified curve, the execution time for low OPA size is
256 negative (-7.601), which is surely impractical. By regionally enlarging Fig. 3(c) into Fig. 3(d),
257 it is seen the fitted curve deviates significantly with the data while the OPA has few elements.
258 We believe at this region, the computation time is not dominated by only the PSO processing.
259 Hence the practical curve behavior should be modified as the pink curve. The main reasons
260 behind may mainly come from the basic computer architecture, including both the hardware
261 and software configurations, which dominate the computation time at less data amount.
262 According to the modified curve, the execution time for OPA size of 128 and 512 will
263 respectively be 209 and 5.25×10^{17} hours. This is surely impractical, and will cast much
264 challenges on the calibration processing. Though in practical systems the expended time may
265 be much reduced (because no needs of transferring and processing a large amount of samples
266 as the numerical emulation does), a faster algorithm is still desirable. The coordinates of Fig.

267 3(c) are extended and shown as Fig. 3(e), which clearly present the curve behaviors of the radix-
268 p methods at larger size of antenna arrays. From Fig. 3(e), it is seen through the proposed radix-
269 p (p ∈ {2, 8, 16}) algorithm, the computation time is much reduced, and the expended time
270 grows linearly (rather than exponentially) with the size of the OPAs. The linear behaviors hold
271 even while the number of antenna elements is as large as 4096, and meet the theoretical
272 prediction. This shows the great performance improvement of the proposed algorithms.

273   In the proposed algorithm, p-element optimization is performed for every sub-set
274 processing. The time expended by the p-element processing is denoted as $O_{\text{p-element}}$. For the
275 whole calibration processing, there are $\log_p(N)$ layers; and for the r-th layer, there is N/p^r sub-
276 set processing. The total expended time is then a geometric series with $\log_p(N)$ terms, and can
277 be derived as:

$$278 \quad O_{\text{p-element}} \sum_{r=1}^{\log_p N} N \cdot p^{-r} + \text{Res.} = O_{\text{p-element}} N \frac{p^{-1}\left(1 - p^{-\log_p N}\right)}{1 - p^{-1}} + \text{Res.} \quad (9)$$

279 A residual (Res.) term is added in Eq. (9) to cover general cases, for which $\log_p(N)$ may be a
280 fractional number. While $\log_p(N)$ is not an integer, the sub-set will be selected at its best
281 possible efforts, and the remaining <p terms will be calculated independently. As the number
282 is less than p, this will not cause much additional computation time. In order to more clearly
283 observe the behavior of the computation time, a factoring function, K(N), is defined from Eq,
284 (9) as:

$$285 \quad K(N) = \frac{p^{-1}\left(1 - p^{-\log_p N}\right)}{1 - p^{-1}}. \quad (10)$$

286 Fig. 4(a) shows the values of K for different N and p. It is observed that while N becomes larger
287 than 4, the ascending rate of K significantly decreases. After N>16, K grows even slower and
288 becomes almost constant (K_c) for all values of p. Hence, Eq. (9) can be approximated as:

$$289 \quad O_{\text{p-element}} \sum_{r=1}^{\log_p N} N \cdot p^{-r} \approx K_c O_{\text{p-element}} N. \quad (11)$$

290 Eq. (11) shows the computation time scales linearly with the number of N. This shows great
291 performance in computation time of the proposed algorithm for the cases of larger N, which
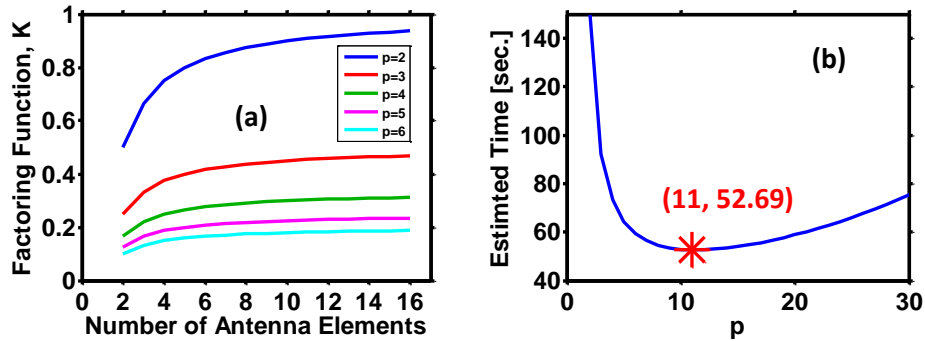292 meets the results of Fig. 3(c).

Fig. 4. (a) The factoring function at different p and OPA size. (b) the estimated time expense for different p.

293   It is noted that $O_{p\text{-element}}$ typically increases with the number of p as shown in Fig. 3(c) and
294   (d). However, as shown in Fig. 4(a), K_c increases with the reduction of p due to the increasing
295   layers and sub-sets at low-p cases. Hence, an optimized p for best reducing the total
296   computation time may commonly be larger than 2. The optimized p is estimated according to
297   the results of Fig. 3(d) and 4(a). Fig. 4(b) shows the estimated time expense for N=64 at
298   different p. It is seen that the time expense can be further reduced while p slightly increases as
299   high as up to 11. After p>11, the time expense of the PSO dominates, and slow down the overall
300   processing speed. Fig. 3(e) shows the simulated time expense for different values of p with the
301   array size up to 4096. Since the computation region must be extended to get finer image
302   resolution for the narrower beam widths of larger array sizes, the computation data points of
303   the radix-p methods are increased by 4 times. This results in about x4 more time expense, which
304   is also observed between the results of Fig. 3(c) and Fig. 4(b). In Fig. 3(e), the lowest time
305   expense is observed at the case of p = 8. For other cases, whether p becomes larger (p=16) or
306   smaller (p=2), the time expense increases as predicted in Fig. 4(b). This suggests the
307   possibilities of further time reduction with more optimized choices of p.
308   Figure 3(f) shows the final average calibrated phase errors for different values of p at
309   different sizes of antenna arrays. For all values of p, higher phase errors are approximately
310   observed while the array sizes increase. This is possibly caused by the numerical errors of each
311   sub-set processing, which are accumulated with more processing stages at large array sizes. For
312   the same array sizes, the final phase errors increase at higher p. This may mainly come from
313   the performance variances of PSO at larger antenna sizes (higher p). As shown in Fig. 3(c), it
314   is seen that the calibration results are sensitive to the number of applied particles. While the
315   applied particles are around the values of the fitting curve, there are possibilities that the
316   converged phase results are not fully optimized. As the array sizes increase, huge variations are
317   observed for the optimized number of particles. Hence, while p increases, there are potentially
318   more errors generated by PSO. This also explains for the fluctuations of phase errors for the
319   p=8 case shown in Fig. 3(f). One insight perceived from the results of Fig. 3 (f) is that: even if
320   p>2 may result in less computation time as illustrated in the last paragraph, it will also introduce
321   further phase errors. Hence, the optimized values of p should also be determined by the
322   tolerable phase errors of the practical systems, and may deviate from the values around 11
323   shown in Fig. 4(b).

324   *3.2 Calibration error*
325   The calibration performance is analyzed for an OPA with 64 elements. Additional noise with
326   normal distribution is added onto the phase term of each antenna element to emulate the
327   possible variations of the control signals during the optimization processing. The standard
328   deviation of the noise is swept from $0\sim2\pi$. The original and the calibrated patterns are
329   respectively shown in Fig. 5(a) and (b), which reveal the monitored region between $\pm1^{st}$ order
330   grating lobes (two FSRs) [16]. The legends for the red and green curves respectively denote for
331   the strength of the added noise in unit of radian. It can be seen that while the control signals do
332   not exhibit additional noise (the red curve), the phase errors are almost correctly calibrated.
333   Hence, the intensity of the main lobe is significantly distinguished, and the SMSR is about
334   13.256 dB. This is a level close to the ideal level of 13.269 dB. We believe the ~0.013 dB
335   penalty is an inherent limitation of the proposed radix-p algorithm. The phases of the antenna
336   elements belonging to different sub-sets are not adjusted simultaneously. Numerical errors exist
337   after each sub-set processing. The errors will propagate to the processing of the succeeding
338   layers, and result in additional calibrated errors compared to the algorithms not applying the
339   radix-p scheme. The errors can also be observed at the edges of Fig. 5(b), for which the red
340   curve is not symmetrical for the lobes ~ 20 dB lower than the main lobe.
341   Figure 5(c) shows the strengths of the main lobe, the maximal side lobe, and the SMSR at
342   different noise levels. As the patterns with poor phase adjustment can be random, the main lobe
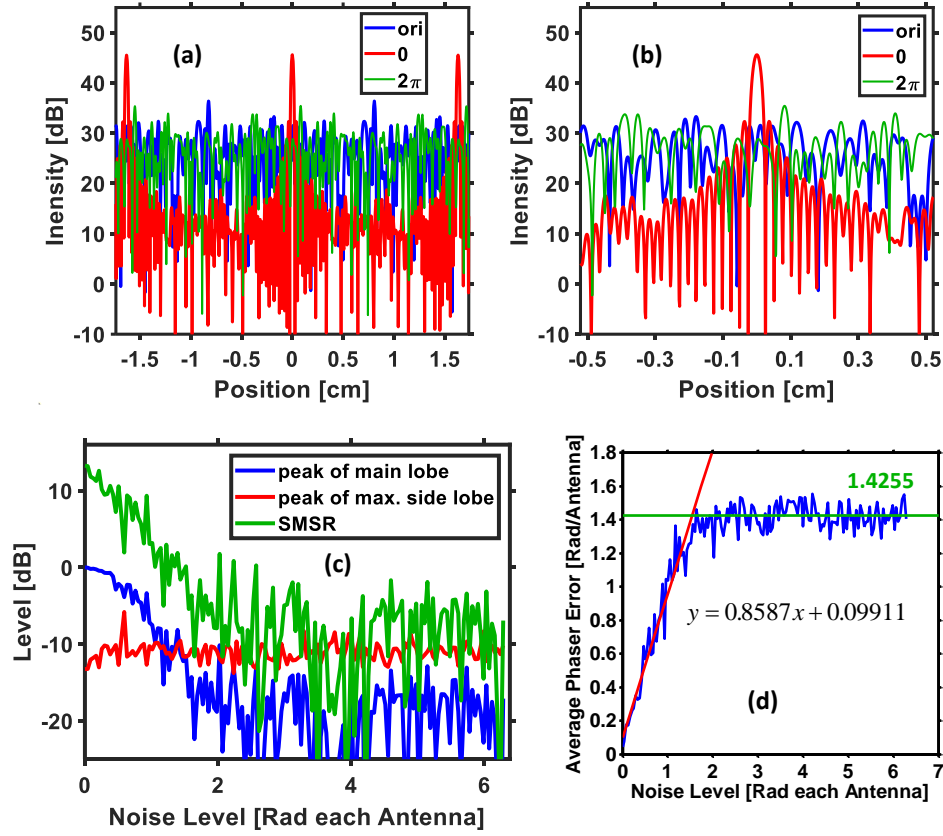
Fig. 5. Calibration performance. (a) Field pattern with wide range. (b) zoomed in plot of (a). (c) Intensity traces of the lobes and SMSR. (d) Calibrated errors. Note: values of (a) and (b) are the strengths of the added noise in radian. Ori: original.

343   is defined as the value observed at the point of interest. It is seen that the intensity of the main
344   lobe and SMSR decrease at higher noise levels of the control signals. While the noise level is
345   higher than ~2 radian, the intensities of the main lobe and the SMSR are at their minimum
346   levels. Hence no benefits are offered by calibration. This phenomenon can be further observed
347   in Fig. 5(b) for the case of 2π noise level. Ripples with no significant lobes are observed as
348   expected.

349   Figure 5(d) shows the average absolute phase errors after the calibration processes. At all
350   noise levels, error floors are observed. An error around 0.043 radian is observed even while the
351   noise is not added. This again can be explained by the numerical errors and the resultant non-
352   ideal SMSR level of 13.256 dB shown in Fig. 5(a)-(c). The error floors increase with the
353   strengths of the noise, and saturate at levels around 1.4255 as labeled by the green line and text.
354   As the maximum value in Fig. 5(d) is 1.5538 (~$\pi/2$), the saturated error levels may result from
355   an un-correlated quadrature condition. It is seen that the saturation point is at the noise level of
356   around 2 radian, which corresponds to the point of the SMSR floor shown in Fig. 5(c). Before
357   the saturation point, the final average phase errors grow linearly with the noise levels of the
358   control signals. The fitting curve is directly shown and labeled on Fig. 5(d). These values
359   indicate the potential strategies to choose different control-signal generators. Assume the
360   control signals are generated through ideal digital-to-analog converters (DACs), which can be
361   adjusted exactly within the 2π range. Then, according to Fig. 5(d), specific calibration benefits

362 can be gained with bit resolution higher than 2. And considering the error floor of 0.043 radian
363 at 0 control noise, DACs with bit resolution around 8 bits may be sufficient to offer performance
364 close to the best available levels.

4. Conclusions

366 An efficient radix-p algorithm is proposed and analyzed. The proposed radix-p algorithm can
367 be combined with most of the existing optimization algorithms as a speedup booster.
368 Theoretical analyses are performed and show that the computation time of the radix-p algorithm
369 grows linearly with the size of the OPAs. This offers great computation improvement, in
370 comparison to the conventional particle swarm optimization (PSO) algorithm exhibiting
371 exponential computation time shown in our numerical results. The processing time and
372 accuracy are analyzed through numerical methods. In the simulation environment, the proposed
373 radix-p processing shows more than 12 times efficiency improvement than the traditional PSO
374 algorithm. The radix-p algorithm may suffer from additional numerical errors, which results in
375 about 0.013 dB SMSR degradation. Considering the existence of the numerical errors, the bit
376 resolution with ~8 may reach performance close to the algorithm's limitation.

Disclosure

381 The authors declare no conflicts of interest.

Data availability

383 Data underlying the results presented in this paper are not publicly available at this time but
384 may be obtained from the authors upon reasonable request.

References

1. K. V. Acoleyen, W. Bogaerts, J. Jágerská, N. L. Thomas, R. Houdré, and R. Baets, "Off-chip beam steering with a one-dimensional optical phased array on silicon-on-insulator," Opt. Lett. **34**(9), 1477-1479 (2009).
2. J. K. Doylend, M. J. R. Heck, J. T. Bovington, J. D. Peters, L. A. Coldren, and J. E. Bowers, "Two-dimensional free-space beam steering with an optical phased array on silicon-on-insulator," Opt. Express **19**(22), 21595-21604 (2011).
3. W. Guo, P. R. Binetti, C. Althouse, M. L. Maanovic, H. P. Ambrosius, L. A. Johansson, and L. A. Coldren, "Two-dimensional optical beam steering with InP-based photonic integrated circuits," IEEE J. Sel. Top. Quantum Electron. **19**(4), 6100212 (2013).
4. J. C. Hulme, J. K. Doylend, M. J. R. Heck, J. D. Peters, M. L. Davenport, J. T. Bovington, L. A. Coldren, and J. E. Bowers, "Fully integrated hybrid silicon two dimensional beam scanner," Opt. Express **23**(5), 5861-5874 (2015).
5. S. Chung, H. Abediasl, and H. Hashemi, "A monolithically integrated large-scale optical phased array in Silicon-on-Insulator CMOS," IEEE JSSC **53**(1), 275-296 (2018).
6. S. A. Miller, C. T. Phare, Y.-C. Chang, X. Ji, O. A. J. Gordillo, A. Mohanty, S. P. Roberts, M. C. Shin, B. Stern, M. Zadka, and M. Lipson, "512-element actively steered silicon phased array for low-power LIDAR," In Proc. CLEO, JTh5C.2. (2018).
7. M. Prost, Y.-C. Ling , S. Cakmakyapan, Y. Zhang ,K. Zhang, J. Hu, Y. Zhang, and S. J. B. Yoo, "Solid-state MWIR beam steering using optical phased array on germanium-silicon photonic platform," IEEE Photon. J. **11**(6), no. 6603909 (2018).
8. R. Fatemi, A. Khachaturian, and A. Hajimiri, "A nonuniform sparse 2-D large-FOV optical phased array with a low-power PWM drive," IEEE JSSC **54**(5), 1200-1215 (2019).
9. C. V. Poulton , M. J. Byrd, P. Russo, E. Timurdogan, M. Khandaker, D. Vermeulen , and M. R. Watts, "Long-range LiDAR and free-space data communication with high-performance optical phased arrays," IEEE J. Sel. Top. Quantum Electron. **25**(5), 7700108 (2019).
10. S. Guerber, D. Fowler, I. Charlet, P. Grosse, K. Abdoul-Carime, J. Faugier-Tovar, and B. Szelag, "Development, calibration and characterization of silicon photonics based optical phased arrays," in Proc. SPIE 11690, Smart Photonic and Optoelectronic Integrated Circuits XXIII, 1169006 (2021).
11. H. Hashemi, "Large-scale monolithic optical phased arrays," in Prof. OFC, Tu3E.5 (2019).

12. T. Komljenovic and P. Pintus, "On-chip calibration and control of optical phased arrays," Opt. Exp. **26**(3), 3199-3210 (2018).

13. Q.-H. Zhang, L.-X. Zhang, Z.-Y. Li, W. Wu, G.-X. Wang, X.-C. Sun, W. Zhao, W.-F. Zhang, "Antenna array initial condition calibration method for integrated optical phased array," Acta Photonica Sinica **49**(7), 726001-0726001 (2020).

14. Y. Shi and R. Eberhart, "A modified particle swarm optimizer," 1998 IEEE International Conference on Evolutionary Computation Proceedings. 69-73 (1998).

15. A. Ratnaweera, S. K. Halgamuge, and H. C. Watson, "Self-organizing hierarchical particle swarm optimizer with time-varying acceleration coefficients," IEEE Transactions on Evolutionary Computation 8(3), 240-255 (2004).

16. B. Abiri, R. Fatemi, and A. Hajimiri, "A 1-D heterodyne lens-free optical phased array camera with reference phase shifting," IEEE Photon. J. 10(5), no. 6601712 (2018).